https://doi.org/10.1016/j.applthermaleng.2022.118454

Hybrid Nanofluid Spray Cooling Performance and its Residue Surface Effects: Toward Thermal Management of High Heat Flux Devices

Farooq Riaz Siddiqui[1], Chi-Yan Tso[2], Huihe Qiu[1], Christopher Y. H. Chao[3], Sau Chung Fu[4*]

[1]Department of Mechanical and Aerospace Engineering, The Hong Kong University of Science and Technology, Hong Kong

[2]School of Energy and Environment, City University of Hong Kong, Hong Kong

[3]Department of Building Environment and Energy Engineering, Department of Mechanical Engineering, The Hong Kong Polytechnic University, Hong Kong

[4]Department of Mechanical Engineering, The University of Hong Kong, Hong Kong

*Corresponding Author Tel.: +852 3910 2154

E-mail Address: scfu@hku.hk

Postal Address: Department of Mechanical Engineering, The University of Hong Kong, Pokfulam Road, Hong Kong

Abstract

In recent years, heat dissipation in high heat flux devices remarkably increased and it is anticipated to reach unprecedented levels in future devices, mainly due to increased power density, compact packaging and high-performance requirements. To address this challenge, in current research, we initially investigate the spray cooling performance and spray residue surface effects of the next generation thermal fluid, called hybrid nanofluid. Subsequently, we investigate the hybrid nanofluid spray cooling potential to address heat dissipation issues in a high heat flux application, that is, the electric vehicle (EV) high power electronics. Our results demonstrate that the critical heat flux (CHF) enhancement up to 126% can be achieved using the hybrid nanofluid spray cooling compared to water spray cooling. The hybrid nanofluid and its spray residue characterization further suggest that high CHF in hybrid nanofluid spray cooling may be due to high latent heat of vaporization and residue wetting and wicking effects. Moreover, the spray cooling efficiency and Nusselt number obtained for hybrid nanofluid spray cooling is more than twice that of water spray cooling. Furthermore, our results indicate that the hybrid nanofluid spray cooling can keep high

power electronics of current and future electric vehicles below their failure temperatures, while the same cannot be achieved using water and dielectric fluid spray cooling.

Keywords: Hybrid nanofluid spray, high heat flux devices, spray residue, EV high power electronics, critical heat flux.

Nomenclature

CAHF	Copper-alumina hybrid nanofluid	*SGHF*	Silver-graphene hybrid nanofluid
CHF	Critical heat flux	T_a	Ambient temperature, K
DBC	Direct bond copper	T_{sat}	Fluid saturation temperature, K
d	Spray droplet diameter, m	T_f	Fluid temperature at nozzle inlet, K
d_{32}	Sauter mean diameter, m	T_{sc}	Critical surface temperature, K
EV	Electric vehicle	T_s	Surface temperature, K
h	Heat transfer coefficient, $Wm^{-2}K^{-1}$	*WBG*	Wide band gap
h_{fg}	Latent heat of vaporization, J/kg	*We*	Weber number
IGBT	Insulated gate bipolar transistor	*Greek Symbols*	
k	Thermal conductivity, $Wm^{-1}K^{-1}$	ϕ	Observation angle
MR	Mixing ratio	$\Delta\phi$	Fringe spacing, m
n	Droplet refractive index	λ	Laser Wavelength, nm
Nu	Nusselt number	φ	Volume fraction
Pr	Prandlt number	γ_{sv}	Surface free energy, N/m
q'	Spray critical heat flux, Wcm^{-2}	$\emptyset_f$	Mean pore diameter, m
Q''	Mean volumetric flux, $m^3m^{-2}s^{-1}$	θ	Static contact angle
R_a	Average surface roughness, m	η	Spray cooling efficiency
Re	Reynolds number		

1. Introduction

Spray cooling is widely used in thermal management of various high heat flux devices, such as electric vehicle (EV) high power electronics, data centers, laser diodes, radars and X-ray machines. Despite other existing cooling techniques, such as microchannel heat sink, jet impingement, heat pipe and pool boiling, spray cooling is still preferred for thermal management of high heat flux devices due to its several benefits, such as, high heat flux removal, uniform surface cooling, no temperature overshoot, small fluid inventory and low flow rates [1–3]. It is the latent heat transfer, low thermal contact resistance and high droplet surface area to volume ratio that make the spray cooling a promising technology for effective cooling of high heat flux devices [4,5]. Moreover, modified surfaces with high roughness and micro/macro structures can further improve heat transfer rates of spray cooling processes [6].

Despite several benefits of spray cooling technology, it may not fully address the emerging heat dissipation issues in modern high heat flux devices. This is because heat dissipation levels in state-of-the-art high heat flux devices tremendously increased in recent years that may not be addressed using existing thermal fluids (such as water and dielectric fluids). For instance, heat dissipation flux in existing EV high power electronics comprising insulated gate bipolar transistor (IGBT) modules can be up to 500 W/cm^2 [7–9].. This may increase up to 1000 W/cm^2 in future EV high power electronics where wide band gap (WBG) modules will replace IGBT modules due to their high power density, reduced power losses and small die size [10,11]. Similarly, high power LEDs have heat dissipation in a range of 250-500 W/cm^2, while high power laser diodes have heat dissipation up to 1000 W/cm^2 [4,12,13]. On the other hand, water and dielectric fluids used in microchannel heat sink, heat pipe, jet impingement and spray cooling technologies can remove heat flux only up to 312 W/cm^2 in currently used IGBT modules [9,14–17]. This shows that the cooling performance of existing heat transfer fluids is much lower than heat dissipation flux of modern high heat flux devices thus pressing an urgent need for advanced thermal fluids, such as nanofluids.

Nanofluids comprise thermally conductive ultra-fine particles suspended in a base fluid, such as water [18]. Nanofluids possess superior thermal properties than their base fluids and may therefore exhibit improved spray cooling performance [19–22]. Hsieh et al. [23] reported an increase in critical heat flux (CHF) up to 2.4 times using silver nanofluid spray cooling compared to water spray cooling. Other researchers also reported similar heat transfer enhancements using less concentrated nanofluids (volume fraction less than 1%) in spray cooling applications. A few researchers also reported a reduction in spray cooling performance with increase in nanofluid concentration [24–26].

Despite enhanced spray cooling performance reported in literature for some nanofluids, they are not suitable for high heat flux cooling applications as they do not possess overall thermofluid characteristics [27–29]. For instance, highly conductive nanofluids (such as copper and silver nanofluids) exhibit low dispersion stability, while stable nanofluids (such as alumina nanofluid) show reduced thermal conductivity. The overall thermofluid characteristics are achieved when highly stable nanoparticles are dispersed along with highly conductive nanoparticles in a base fluid to obtain a hybrid nanofluid exhibiting high dispersion stability and enhanced thermal conductivity. The hybrid nanofluid is the next generation heat transfer fluid and is synthesized by dispersing two different types of nanoparticles in the base fluid. The hybrid nanofluids outperform single particle nanofluids mainly due to their better hydrothermal characteristics (high stability and enhanced thermal properties) and synergistic thermal effects [30–32]. The two different types of nanoparticles in hybrid nanofluids act as thermal pathways lowering the thermal contact resistance among similar nanoparticles that results in synergistic thermal effect [33,34]. These properties make hybrid nanofluids potential heat transfer candidates for spray cooling of high heat flux devices. Despite potential benefits of hybrid nanofluids over single particle nanofluids or base fluids, the hybrid nanofluid spray cooling performance has not been investigated to date.

The main focus of this study is to investigate the spray cooling performance of the copper-alumina hybrid nanofluid (CAHF) and the silver-graphene hybrid nanofluid (SGHF) for volume fraction in a range of 0.01−1%. In this study, the CAHF was used at a fixed mixing ratio of 0.5(Cu):0.5(Al_2O_3), while the SGHF was used at two different mixing ratios (MR) of SGHF/MR-1 as 0.1(Ag):0.9(GNP) and SGHF/MR-2 as 0.9(Ag):0.1(GNP). This is because the CAHF exhibits enhanced overall hydrothermal characteristics for a mixing ratio of 0.5(Cu):0.5(Al_2O_3) [30], while the SGHF shows enhanced droplet evaporation rate at mixing ratios of 0.1(Ag):0.9(GNP) and 0.9(Ag):0.1(GNP) for sub-boiling and nucleate boiling temperatures, respectively [35]. In current research, the spray cooling performance of these three hybrid nanofluids (CAHF, SGHF/MR-1 and SGHF/MR-2) was investigated and compared with the benchmark fluid (water). Subsequently, the residue formed over the heater surface was examined and its effect on the critical heat flux (CHF) enhancement of the hybrid nanofluid spray cooling was investigated.

Besides hybrid nanofluid spray cooling performance, in this research, the hybrid nanofluid spray cooling potential for thermal management of electric vehicle (EV) high power electronics was also investigated and compared with water and dielectric fluid (FC-72 and HFE-7100) spray cooling. A typical power electronics module comprises a switching device (electronic chip) soldered to a substrate (copper) collector carrying high voltages and high current. This configuration has a low package thermal resistance, as only a single copper layer is used as a substrate. Also, the dielectric coolant must be used in this configuration, as the fluid comes in direct contact with the copper substrate. Although deionized water is a dielectric medium and used as a base fluid for hybrid nanofluid synthesis in this research, the suspended hybrid nanoparticles in it may transform it into an electrically conductive medium, making it unsafe for direct cooling of EV power electronic modules. Therefore, in this research, the hybrid nanofluid spray cooling was also investigated for another configuration in which a direct bond copper (DBC) was used as a substrate due to its high electrical insulation and enhanced thermal conduction properties. The direct bond copper comprises a layer of ceramic material sandwiched between two copper layers. The ceramic material acts as a dielectric medium between the two copper layers and provides an electrical insulation to the lower copper layer from the top copper layer handling high voltages. Alumina (Al_2O_3) is the most commonly used ceramic material in DBC substrates [14,36]. Despite its promising dielectric properties, it increases the package thermal resistance due to its low thermal conductivity. Therefore, in this research, aluminum nitride (AlN) was used in the DBC, as it is an excellent electrical insulator and is about eight times more thermally conductive than Al_2O_3 [36,37]. In this DBC based packaging, the lower copper layer below the ceramic layer was cooled using the hybrid nanofluid spray. Moreover, in this research, the thermal management of insulated gate bipolar transistor (IGBT) module that is currently used in EV high power electronics was initially investigated. Subsequently, the thermal management of wide band gap (WBG) module to be used in future EV high power electronics was studied using the hybrid nanofuid spray cooling. This study has the following objectives:

- To investigate and compare the hybrid nanofluid spray cooling performance with water spray cooling performance.
- To study the effect of hybrid nanofluid spray residue on critical heat flux enhancement.
- To investigate the cooling potential of hybrid nanofluid spray cooling for power electronics thermal management of current and future electric vehicles.

2. Experimental methodology

2.1. Hybrid nanofluid spray cooling setup and procedure

In this research, the hybrid nanofluids were prepared by a two-step method in which two different types of nanoparticles were dispersed in water followed by ultrasonication. Subsequently, the latent heat of vaporization for studied hybrid nanofluids (as shown in Table 1) was measured using a differential scanning calorimetry (Q1000, TA instruments, USA) with maximum uncertainty (mean standard deviation) of 59.5 kJ/kg. The experimental uncertainty was determined from mean standard deviation of repeated measurements in this research. Although adding hybrid nanoparticles increases the viscosity of hybrid nanofluids that may result in pumping losses and pipe clogging issues, high latent heat of vaporization is obtained for considered hybrid nanofluids at low particle loading of 0.1% volume fraction, (as shown in Table 1). Moreover, at low particle loading , the hybrid nanofluid viscosity enhancement is negligible with significant increase in thermal conductivity as compared to that of water, as reported in our study [30].

An experimental setup was developed to investigate and compare the hybrid nanofluid spray cooling performance with water spray cooling performance under similar ambient conditions at a constant ambient temperature (T_a) of 25 °C, as illustrated in Figure 1 (a). The copper cylinder (32 mm × 190 mm) was used as a heater that comprised two parts, the heater body with a large (32 mm) diameter and the heater head with a small (10 mm) diameter. The flat surface on heater head was used as a heater spray surface, as demonstrated in Figure 1 (a). Four holes, each separated by vertical distance of Δy = 5 mm, were bored along the heater head sidewall. A T-type thermocouple (0.2 mm diameter) was inserted in each hole for temperature measurements T_1, T_2, T_3 and T_4, where temperature T_1 was measured closest to the heater surface while temperature T_4 was measured farthest from the heater surface. The temperature data from thermocouples was obtained every second using the data acquisition card (Model: 9171, National Instruments, Hungary) and the measured temperature was used to determine the spray cooling heat flux based on the Fourier's law of heat conduction ($q = kA\Delta T/\Delta y$). The heater surface temperature (T_s) was determined from linear extrapolation of temperature data obtained from thermocouples along the heater head side wall using the relation $T_s = T_1+[\Delta y_{s-1}/\Delta y_{4-1}](T_4-T_1)$, where Δy_{s-1} is the vertical distance between the heater surface (T_s) and thermocouple T_1 while Δy_{4-1} is the vertical distance between thermocouple T_4 and thermocouple T_1. Moreover, the experimental uncertainty in spray cooling heat flux was determined as mean standard deviation from three heat flux values measured from four thermocouples along the heater head sidewall. The cartridge heater (1 kW, 16 mm ×160 mm) was inserted in a hollow heater body to heat the copper heater spray surface (10 mm diameter). The cartridge heater base was enclosed in a metal cap that was screwed on the heater body sidewall. The copper heater sidewall was insulated with the super-wool thermal insulation sheet to minimize heat losses. The heater head was inserted through the Teflon base of the spray chamber such that the heater spray surface was aligned with the Teflon surface. The high temperature silicone was applied on heater head sidewall before insertion into the Teflon base to prevent any leakages during the spray cooling experiment. The spray chamber comprised a Teflon base with the heater spray surface positioned at its center, while the sidewalls and the top plate were made of polydimethylsiloxane (PDMS).

The spray nozzle (1/4 T-SS+TG-SS 0.3, Spraying Systems, USA) with an orifice diameter of 508 μm was inserted into a spray chamber through a hole at the center of the top plate such that the nozzle was aligned perpendicular to heater spray surface. The nozzle height (distance between the nozzle tip and the copper heater surface) was fixed at 20 mm so that the nozzle spray full cone covered the entire copper heater surface. To prevent nozzle clogging, stainless steel mesh (mesh size = 0.15 mm) was used at nozzle inlet. As hybrid nanofluid spray droplets impacted the heater surface, a stream of hybrid nanofluid entered the plate heat exchanger (LBP410-040, Xylem, UK), where it was cooled by water in a cooling loop. The water temperature in a cooling loop was fixed at 20 °C using a circulation bath. On heat exchanger exit, the cold hybrid nanofluid stream entered the fluid storage tank. The hybrid nanofluid from fluid storage tank was pumped into the spray chamber using a 54 W (DC) centrifugal pump (Model: 083942, Xylem Flojet, UK). The pump was turned on 10 minutes before switching on the heater to avoid fluctuations induced by the pump. The pressure gauge was used at spray chamber inlet to monitor the spray n, while the volumetric flow rate was measured using a variable area flow meter (Model: 2510A2A12BVBN, Instruments Direct, USA).

In the spray cooling experiment, one-liter hybrid nanofluid was poured into the fluid storage tank. The pump was turned on and the hybrid nanofluid was sprayed on the heater spray surface. As the spray system reached a steady state in about 5 minutes, the heater was turned on at a low AC voltage of 50 V. The increasing temperature along the heater head sidewall was monitored using thermocouples and it reached a steady state (almost constant temperature) in 45-60 minutes. The steady state temperature was recorded and the voltage was increased from 50 V to 70 V. It took another 45-60 minutes for the spray system to reach a steady state temperature. The same procedure was repeated with 20 V increment until the point of the critical heat flux (CHF). At CHF, the heater was immediately turned-off to prevent heater burnout due to the temperature overshoot. The hybrid nanofluid spray system continued working until the heater surface was cooled around the room temperature. Subsequently, the temperature data from two consecutive thermocouples along the heater head sidewall was processed to determine the heat flux using the thermal conductivity for copper as 393 W/(m.K) [38]. As four thermocouples were used along the heater head sidewall, three heat fluxes were determined and the average heat flux was reported in section "Results and discussion". The maximum uncertainty (mean standard deviation) in critical heat flux was determined as 35 W/cm^2. Moreover, the heater spray surface temperature was determined by extrapolating the measured temperature along the heater head sidewall. The spray cooling experiments were performed at the mean volumetric flux of Q'' = 0.01 m^3/(m^2.s) and 0.019 m^3/(m^2.s), where the mean volumetric flux is defined as the spray volumetric flow rate divided by the spray impact area on heater surface [5]. Mean volumetric flux of 0.019 m^3/(m^2.s) corresponding to pump pressure of 0.143 MPa was the maximum achievable value for the pump (54 W maximum power) used in this experimental setup. On the other hand, mean volumetric flux of 0.01 m^3/(m^2.s) corresponding to 0.129 MPa was the lowest achievable value in this developed experimental setup. For Q'' < 0.01 m^3/(m^2.s), the spray nozzle ejected a continuous stream of fluid and did not break as fine droplets. After each experiment, the residue formed on a copper spray surface was cleaned using a sand paper and subsequently polished using a (Brasso) metal polish.

2.1.1. Spray characterization

The spray droplet velocity field and the spray droplet size distribution were measured using LaVision's particle master interferometric Mie imaging (IMI) system that is also compatible with LaVision's flow master particle image velocimetry (PIV) system. Among a wide range of applications, LaVision's IMI and PIV systems also cover spray droplet investigations. For PIV measurements, spray droplets were illuminated by Nd:YAG laser sheet. The light intensity scattered by spray droplets was recorded by CCD camera. The distance between the CCD camera and the spray nozzle was adjusted to 80 cm while the distance between the laser and the spray nozzle was adjusted to 23 cm. These distances were adjusted to get the required field of view and laser sheet intensity for spray droplet image acquisition. The angle between the laser and CCD camera was set to 90° and the camera lens zoom factor was adjusted to 1:1. The time delay for the double exposure laser was 50 μs and total 10 images were acquired at 5 frames per second. The mean velocity field based on all 10 images was developed using Tecplot.

For spray droplet size measurements, defocused Mie imaging technique was used in LaVision's IMI system that generated fringe patterns from spray droplets, where fringe spacing is inversely related to droplet diameter. For IMI measurements, the distance between the CCD camera (same zoom factor of 1:1 as set in PIV measurements) and the spray nozzle was adjusted to 12 cm while the laser-camera angle was adjusted to 60° in order to obtain the interference fringes. The distance between the laser and the spray nozzle was the same (23 cm) as in PIV measurements. The rectangular aperture was mounted on the CCD camera due to high spray droplet density. In these experiments, total 90 images were acquired at 5 frames per second using a single exposure laser pulse. These images were subsequently processed to obtain the spray droplet size distribution. The aperture image finding algorithms in IMI software determines the aperture image size, position, angle and its intensity profile. Subsequently, the intensity mapping is performed in IMI software by counting the number of intensity maxima. Finally, with known observation angle (ϕ), fringe spacing ($\Delta\phi$), droplet refractive index (n) and laser wavelength (λ), the spray droplet diameter was determined in IMI software based on the relation $d = 2\lambda/\Delta\phi\left[cos\left(\frac{\phi}{2}\right) + nsin\left(\frac{\phi}{2}\right)/\sqrt{1 + n^2 - 2ncos(\frac{\phi}{2})}\right]^{-1}$. As hybrid nanofluids are opaque and may not possess required optical properties for PIV and IMI measurements, the spray velocity field and droplet size distribution experiments were performed for only water spray. However, due to low particle loading of 0.01-1% volume fraction, hybrid nanofluid spray characteristics may resemble that of water. Furthermore, Panão et al. [39] showed that nanoparticles have a negligible effect on spray structure of base fluid spray systems.

2.2. Hybrid nanofluid residue surface characterization

2.2.1. Residue development

The surface properties of the residue developed on a heater surface at the end of hybrid nanofluid spray cooling experiments could not be subsequently examined. This is because the limited test section space in surface characterization equipment (such as optical profiler, optical tensiometer and SEM) could not accommodate large heater body used in current spray cooling experiments. Also, repetitive assembling and disassembling of heater body for residue characterization would affect the repeatability of spray cooling tests. Therefore, separate experiments were conducted for residue surface measurements. A copper plate with dimensions of 10 mm (length) × 10 mm (width) × 3 mm (height) and having the same surface area as the heater head (used in spray cooling) was heated up to the surface temperature of 100 °C on a 100 W silicone heater mat (RS, UK). A 150 µl volume of the hybrid nanofluid droplet was dispensed on a heated copper plate. As evaporation ended, a porous residue was formed on the copper plate.

2.2.2. Residue wetting, surface free energy, roughness and porosity tests

Once the hybrid nanofluid droplet residue was developed on a copper substrate, the residue wetting and surface free energy was investigated using the optical tensiometer (Theta, Biolin Scientific, Finland), the residue roughness was studied using an optical profiler (NPFLEX, Bruker, USA) and residue pore structure were examined using a scanning electron microscope (TM 3030, Hitachi, Japan). The maximum uncertainty (mean standard deviation) in residue average surface roughness and mean pore diameter was measured as 0.8 µm and 0.031 µm, respectively. In residue wetting tests, a 3 µl hybrid nanofluid droplet was dispensed on a residue surface and the static contact angle (with maximum mean standard deviation of 1.88°) was measured once the droplet spreading stopped at macroscopic scale (at t = 7s). For surface free energy measurements, a 3 µl droplet of water and diiodomethane was dispensed over the residue surface to measure the static contact angle (at t = 7s) and a widely used OWRK/FOWKES approach was used for surface free energy determination. The maximum uncertainty (mean standard deviation) in surface free energy measurements was 1.98 mN/m. Each experiment was repeated three times to improve accuracy in results. Although spray impact in hybrid nanofluid spray cooling may result in different residue patterns on a heater surface than that obtained in droplet deposition approach (as discussed in Section 2.2.1), both residue surfaces comprise the same hybrid nanoparticles with similar chemical composition. Moreover, in droplet deposition approach, a large hybrid nanofluid droplet of 150 µl volume was dispensed to cover the entire heater surface similar to a spray process, where the heater surface was also fully covered by hybrid nanofluid full spray cone. Furthermore, to keep thermal conditions similar to spray cooling process, the copper plate was heated to 100 °C in droplet deposition approach.

2.2.3. Residue wicking tests

The residue wicking tests were performed on hybrid nanofluid droplet residues developed for surface characterization using a glass capillary tube (length = 150 mm, inner diameter = 0.5 mm, outer diameter = 1mm) and a high-speed camera (HG-100K, Redlake, USA). In order to avoid clogging of hybrid nanoparticles along a thin capillary tube, water was used in wicking tests inside the capillary tube instead of the hybrid nanofluid. It is reasonable to replace hybrid nanofluid with water inside the capillary tube due to negligible difference in viscosity and surface tension (as reported in our recent research [30,40]) at low particle loading of 0.1% volume fraction used in wicking tests. A glass capillary tube was attached to graduated metal scale and mounted on a tripod stand. The capillary tube was immersed in a 50 ml beaker containing water in it such that water rose almost halfway up the capillary tube. Subsequently, the residue sample was placed on a scissor lift platform underneath the capillary tube. A high-speed camera was horizontally positioned such that it was the same level as the lower end of the capillary tube. A high-speed camera was turned-on and the height of the scissor lift having a residue sample on its platform was gradually increased until the residue sample touched the capillary tube lower end. As a result, the water level decreased in the capillary tube due to porous residue wicking effect. The video for decreasing water height inside the capillary tube was recorded for 110 s at a frame rate of 25 frames per second (with horizontal and vertical resolution set as 96 dpi). The same procedure was repeated for different hybrid nanofluid residue samples.

3. Numerical simulation

The temperature distribution across different layers of spray cooled EV power electronics module was investigated using the *heat transfer in solids* interface in COMSOL Multiphysics. The heat transfer process in COMSOL Multiphysics was modelled based on the energy equation $\rho C_p V.\nabla T = \nabla.(k\nabla T) + Q + Q_{ted}$, where C_p is the specific heat capacity, ρ is the density, k is the thermal conductivity and V is the velocity term. Moreover, Q and Q_{ted} are the energy generation and thermo-elastic damping terms, respectively. Both 2-D (single chip package) and 3-D (inverter leg) models were developed in COMSOL Multiphysics using dimensions as available in literature [14] (as shown in Figure 1 (b-d)). It should be noted that the backside in a 3-D model is not a complete spraying surface and it is only an area corresponding to the chip surface area of 1 cm x 1cm, as illustrated in Figure 1 (d). The natural (air) convective cooling with a heat transfer coefficient of h_{air} = 10 W/m^{2}K [41] was applied at the chip upper face while the power electronics package was thermally insulated on sidewalls. The spray heat transfer coefficient h (W/m^{2}K) obtained from our experimental study was used as a boundary condition at the base (lower face) of DBC (backside in a 3-D model). The heat transfer coefficient h (W/m^{2}K) corresponding to the critical heat flux (CHF) was obtained using $h = q'/\Delta T$, where q' is the spray critical heat flux and ΔT is the difference between saturation temperature (T_{sat}) and nozzle inlet temperature (T_f). Both spray critical heat flux (q') and ΔT for water and hybrid nanofluids were obtained from our spray cooling experiments, while data for dielectric fluids was obtained from literature [9,42]. A stationary solver at a relative tolerance of 0.001 was used to obtain steady-state temperature distribution in EV power electronics module. It must be noted that both IGBT and WBG power modules were modelled in a similar way, however, a heat source value of 500 W/cm^2 was used for IGBT chip modelling while 1000 W/cm^2 was used for WBG chip modelling. The 2-D model of a single chip package comprised 1307 triangular grid elements, while a 3-D model of an inverter leg comprised 252150 tetrahedral grid elements and 116434 grid elements. Our experimental data cannot be used for model validation, as our experiments did not measure the temperature distribution in IGBT and WBG chips. For this reason, the numerical model was developed in this research to estimate the temperature distribution in such devices that could not be obtained in our experiments. Moreover, the model validation was not performed as the temperature distribution in EV power electronics module was investigated using a well-known Fourier's law of heat conduction in our model.

4. Results and discussion

4.1. Spray velocity field and spray droplet size distribution

Figure 2 (a) and (b) demonstrate the velocity field of water spray droplets in a region between the nozzle tip and the copper heater surface at a mean volumetric flux of Q'' = 0.01 $m^3/(m^2.s)$ and Q'' = 0.019 $m^3/(m^2.s)$, respectively. At a mean volumetric flux of Q'' = 0.019 $m^3/(m^2.s)$, it is noticed that spray droplets show higher velocity magnitude with the peak velocity of 5.5 m/s compared to the peak velocity of 3 m/s at a mean volumetric flux of Q'' = 0.01 $m^3/(m^2.s)$. Moreover, the streamlines follow a unidirectional trajectory and the spray droplets uniformly spread over the heater surface at a mean volumetric flux of Q'' = 0.019 $m^3/(m^2.s)$. Also, at a mean volumetric flux of Q'' = 0.019 $m^3/(m^2.s)$, spray droplets show high velocity magnitude near the center of the copper heater and reduces radially along the heater surface. Conversely, at a mean volumetric flux of Q'' = 0.01 $m^3/(m^2.s)$, the streamlines are irregular, and the spray droplets do not uniformly spread over the heater surface. As a result, half of the spray domain near the heater surface exhibits high velocity while the other half shows low velocity magnitude.

The spray droplet size distribution for mean volumetric flux of Q'' = 0.01 $m^3/(m^2.s)$ and Q'' = 0.019 $m^3/(m^2.s)$ is illustrated in Figure 3 (a) and (b), respectively. It can be observed that both Figure 3 (a) and (b) exhibit right skewed distribution (as shown by red line in Figure 3 (a) and (b)), where 60-65% of spray droplets have size below 50 µm for studied mean volumetric fluxes. Also, maximum number of droplets are in a size range of 26-50 µm followed by a size range of 0-25 µm and 51-75 µm for both mean volumetric fluxes. This indicates poly-disperse spray droplets that may result in residues comprising various sizes over the heated substrate in the hybrid nanofluid based spray system. Moreover, the number of fine spray droplets (below 50 μm size) at a mean volumetric flux of $Q'' = 0.019$ m^3/(m^2.s) is 6-7 times than that obtained at a mean volumetric flux of $Q'' = 0.01$ m^3/(m^2.s). This suggests a dense flow of fine spray droplets is obtained at a mean volumetric flux of $Q'' = 0.019$ m^3/(m^2.s) compared to that at $Q'' = 0.01$ m^3/(m^2.s). Moreover, large class size in spray droplet size distribution is possibly due to continuous break up and coalesce of spray droplets before having an impact on a heater surface resulting in varying spray droplet sizes.

4.2. Hybrid nanofluid spray cooling performance

Figure 4 (a), (b) and (c) show the heat flux of the SGHF/MR-1, SGHF/MR-2 and CAHF spray cooling systems for mean volumetric flux of $Q'' = 0.01$ m^3/(m^2.s), respectively. The spray cooling heat flux for different volume fractions of the SGHF/MR-1 (φ = 0.01-1%) is compared with the benchmark fluid (water). It is observed that the SGHF/MR-1 spray system shows critical heat flux (CHF) enhancement by 67%, 86%, 55% and 89% for volume fraction of 0.01%, 0.1%, 0.5% and 1%, respectively, as compared to the water spray system, as illustrated in Figure 4 (a). Relatively lower CHF enhancement at 0.5% volume fraction compared to other volume fractions suggest that the hybrid nanofluid thermal conductivity does not much affect the CHF enhancement, as the hybrid nanofluid thermal conductivity increases with increasing volume fraction. Some other factors, such as the residue wetting and wicking effects, may influence the CHF enhancement at different particle concentrations. Moreover, the SGHF/MR-1 spray setup exhibits higher critical surface temperature (T_{sc}) for all studied volume fractions than water spray setup. The critical surface temperature (T_{sc}) is defined as the copper heater surface temperature at which the CHF is achieved. The reason for high critical surface temperature in SGHF/MR-1 spray system can be the high wettability of the MR-1 droplet residue (as shown in Table 2) that keeps the heater surface wetted, thus delaying the CHF to high temperatures.

Figure 4 (b) demonstrates heat flux for different volume fractions of the SGHF/MR-2 spray system in comparison to that of water spray system at a mean volumetric flux of $Q'' = 0.01$ m^3/(m^2.s). It can be noticed that the CHF enhancement in SGHF/MR-2 spray system for volume fractions of 0.01%, 0.1%, 0.5% and 1% is 55%, 52%, 106% and 71%, respectively, as compared to the water spray system. Moreover, the SGHF/MR-2 spray system for all volume fractions exhibits higher critical surface temperature (T_{sc}) than water spray system at studied mean volumetric fluxes. This indicates that a partially wetted residue surface (as shown in Table 2) obtained from the SGHF/MR-2 spray droplets keep the heater surface wetted thus delaying the CHF to high heater surface temperatures. Moreover, significantly high critical surface temperature (T_{sc} > 300 °C) is observed for volume fraction $\varphi \geq 0.5$. This is because a partially wetted residue with high porosity may have resulted due to high concentration of hybrid nanoparticles in SGHF/MR-2 spray droplets. High residue porosity facilitates wetting of the heater surface by allowing spray penetration from top residue layers to its bottom layers thus resulting in high critical surface temperatures. In Figure 4 (c), it is noticed that the CHF in CAHF spray system increases by 52%, 107%, 67% and 93% for volume fractions of 0.01%, 0.1%, 0.5% and 1%, respectively, as compared to water spray system at a mean volumetric flux of $Q'' = 0.01$ m^3/(m^2.s).

Figure 5 (a) demonstrates that the CHF in SGHF/MR-1 spray system at a mean volumetric flux of $Q'' = 0.019$ m^3/(m^2.s) increases by 27.8%, 31.5%, 30% and 26% at volume fractions of 0.01%, 0.1%, 0.5% and 1%, respectively, as compared to the water spray system. However, unlike mean volumetric flux of $Q'' = 0.01$ m^3/(m^2.s), the critical surface temperature (T_{sc}) for 0.01% and 1% volume fractions of SGHF/MR-1 spray system is below that of water spray system at a mean volumetric flux of $Q'' = 0.019$ m^3/(m^2.s). This shows that low T_{sc} can be obtained at high mean volumetric fluxes in the SGHF/MR-1 spray system. Figure 5 (b) illustrates that the CHF enhancement for the SGHF/MR-2 spray system compared to the water spray system at volume fractions of 0.01%, 0.1%, 0.5% and 1% is 26%, 126%, 102% and 84%, respectively, at a mean volumetric flux of $Q'' = 0.019$ m^3/(m^2.s).

Figure 5 (c) shows that at a mean volumetric flux of $Q'' = 0.019$ m^3/(m^2.s), the CHF in CAHF spray system increases by 69%, 100%, 65% and 81% for volume fractions of 0.01%, 0.1%, 0.5% and 1%, respectively, as compared to water spray system. Moreover, a higher critical surface temperature (T_{sc}) for all volume fractions of the CAHF spray setup is observed compared to water spray cooling setup at studied mean volumetric fluxes. This suggests that the partially wetted residue surface (as shown in Table 2) in the CAHF spray cooling system delays the CHF to high surface temperatures as compared to a non-wetted copper surface in water spray cooling setup. Moreover, for sub-boiling temperatures, the liquid film formed from the impact of spray droplets increases the convection heat transfer rate. However, in the nucleate boiling regime, the vapor formed at the liquid-heater interface due to high surface temperatures separate apart the liquid film. Despite reduced liquid film contact area with the heater surface, the heat flux tremendously increases in the nucleate boiling regime. This is due to low thermal contact resistance resulting from reduced film thickness in the nucleate boiling regime. Moreover, spray droplets directly impact the vapor active zones on heater surface resulting in high heat transfer rates in the nucleate boiling regime.

Figure 6 (a) and (b) show the critical heat flux (CHF) and critical surface temperature (T_{sc}) for various volume fractions of SGHF/MR-1, SGHF/MR-2 and CAHF spray cooling systems at mean volumetric flux of $Q'' = 0.01$ m^3/(m^2.s) and $Q'' = 0.019$ m^3/(m^2.s), respectively. It can be observed that increasing the volume fraction up to 0.1% increases the CHF for all studied hybrid nanofluid spray cooling systems. However, further increasing the volume fraction has no considerable effect on the spray cooling performance. This suggests that the hybrid nanofluid high thermal conductivity may only improve the CHF up to the volume fraction of 0.1% and that other factors (such as residue wetting and wicking effects) may dominate the thermal conductivity effect on further increasing the hybrid nanofluid volume fraction. The low CHF at 1% volume fraction may be due to lower latent heat of vaporization (h_{fg}) as compared to other volume fractions for studied hybrid nanofluids, as shown in Table 1. However, the effect of latent heat of vaporization on the CHF is not very clear for other volume fractions of the hybrid nanofluid spray system. Furthermore, the critical surface temperature (T_{sc}) in the SGHF/MR-2 spray setup considerably increases for volume fraction of $\varphi \geq 0.5$, as illustrated in Figure 6 (a) and (b). This is because high nanoparticle concentration may obstruct droplet entrainment across the porous residue layers thus inhibiting complete wetting of the heater surface. However, the heater surface may still be partially wetted such that the CHF delays to high surface temperatures.

The CHF enhancement obtained for SGHF/MR-2 and CAHF spray systems compared to H_2O spray system is 126% and 100%, respectively. This is due to significantly enhanced spray heat transfer coefficient achieved for SGHF/MR-2 and CAHF spray systems as compared to H_2O spray system, as shown in Table 3. Furthermore, both SGHF/MR-2 and CAHF spray systems exhibit significantly higher spray cooling efficiency [$\eta = q'/\rho_f Q''(h_{fg} + C_p \Delta T)$] compared to H_2O spray system, as shown in Table 4. This further suggests that SGHF/MR-2 and CAHF are potential candidates for spray cooling application of modern high heat flux devices compared to H_2O and dielectric coolants. The higher spray efficiency for hybrid nanofluid sprays is mainly due to their significantly higher CHF compared to water spray system. On the other hand, the overall low spray cooling efficiency (η<15%) in this study is possibly due to high spray Weber number $We \sim 10^{-3}$, as spray Weber number is inversely related to spray cooling efficiency [42]. Estes and Mudawar [42] showed that spray cooling efficiency (η) nearly 100% can be achieved for spray Weber Number $We < 10^{-5}$ while it drops to less than 10% for $We \sim 10^{-1}$. In this study, the Weber number was determined using a relation $We = \rho_f Q''^2 d_{32}/\sigma$, where ρ_f is the fluid density, Q'' is the mean volumetric flux, σ is the fluid surface tension and d_{32} is the Sauter mean diameter. The Sauter mean diameter is defined as the droplet diameter with same volume to area ratio as that of the entire spray [43]. In this study, the Sauter mean diameter was determined from the spray droplet size distribution (as shown in Figure 3) using the relation $d_{32} = \sum_i n_i {d_i}^3 / \sum_i n_i {d_i}^2$.

The Nusselt number (Nu) obtained for both SGHF/MR-2 and CAHF spray systems is more than twice that of H_2O spray system, as shown in Table 4. The Nusselt number was determined using the relation $Nu = hd_{32}/k$, where h is the fluid heat transfer coefficient, k is the fluid thermal conductivity and d_{32} is the Sauter mean diameter. The Nusselt number for SGHF/MR-2, CAHF and H_2O spray systems was also estimated using different correlations, as shown in Table 4. It can be noticed that correlation developed by Rybicki and Mudawar [44], and Cho and Ponzel [45] can closely predict the Nusselt number for both SGHF/MR-2 and CAHF spray systems compared that proposed by Mudawar and Valentine [46]. Also, these correlations cannot predict the Nusselt number obtained for H_2O spray system in this study. This is because spray cooling is a complicated process involving various parameters, such as spray nozzle type and orientation, nozzle size, nozzle height to heated surface, spray mean volumetric flux, spray velocity, spray droplet size distribution, fluid type and its thermophysical properties.

4.3. Hybrid nanofluid spray residue wetting and wicking effects

As high CHF is obtained at a low volume fraction of 0.1%, the hybrid nanofluid droplet residue properties were further investigated for 0.1% volume fraction, as shown in Table 2. Despite high surface wetting was observed for SGHF/MR-1 droplet residue, the SGHF/MR-1 spray system does not exhibit high CHF at 0.1% volume fraction. Moreover, the SGHF/MR-2 spray system that gives the highest CHF at a mean volumetric flux of Q'' = 0.019 $m^3/(m^2.s)$ (Figure 6 (b)) has a corresponding less wetted residue surface. This indicates that factors other than the residue wettability, such as the residue wicking effect, may also affect the CHF in hybrid nanofluid spray cooling system. The small pore diameter in SGHF/MR-2 and CAHF residue surfaces (as shown in Table 2) suggest a higher capillary effect than the SGHF/MR-1 residue surface that may have a dominant effect on CHF of SGHF/MR-2 and CAHF spray cooling systems. The small mean pore size of the SGHF/MR-2 and CAHF droplet residues as compared to the SGHF/MR-1 droplet residue is also demonstrated in Figure 7 (a-c). The small pore size of the SGHF/MR-2 and CAHF residue surfaces may facilitate the capillary flow that keeps the heater surface wetted resulting in high CHF, as shown in Figure 6 (b).

Figure 7 (d) illustrates the wicking effect for SGHF/MR-1, SGHF/MR-2 and CAHF residues obtained from their respective 150 µl volume droplets at 0.1% volume fraction. As the wicking effect was negligible for residue obtained from a single hybrid nanofluid droplet, these results are not reported in Figure 7 (d). It is noticed that surface wickability (or wicking distance) considerably increases with increasing number of CAHF droplets (from 2 droplets to 5 droplets) that were used to develop a residue surface. A similar trend is also observed for the SGHF/MR-1 droplet residue. This may be due to increase in residue thickness with increasing number of hybrid nanofluid droplets used to develop a residue surface. However, the wicking effect in the CAHF droplet residue is much pronounced with increasing number of droplets (or residue thickness) as compared to the SGHF/MR-1 residue. This may be due to the smaller mean pore size of the CAHF droplet residue that wicks more fluid than the SGHF/MR-1 droplet residue. Furthermore, in the SGHF/MR-2 droplet residue, the wicking effect (or wicking distance) increases with increasing number of SGHF/MR-2 droplets from 2 droplets to 3 droplets that were used to develop the residue. This may be due to increased residue thickness and pore density resulting in enhanced wicking effect. However, increasing the number of SGHF/MR-2 droplets from 3 droplets onwards decreases the residue wicking effect. This suggests that the mean pore size in the SGHF/MR-2 droplet residue changes with increasing residue thickness that eventually alters its surface wickability. Moreover, these results suggest that enhanced CHF in CAHF and SGHF/MR-2 spray cooling systems (as shown in Figure 6 (b)) at 0.1% volume fraction is due to higher wickability (or wicking distance) of CAHF and SGHF/MR-2 droplet residues as compared to SGHF/MR-1 droplet residue. However, high CHF of SGHF/MR-1 spray cooling setup at low volume fraction (as shown in Figure 6 (a)) suggests that the residue wettability and wickability both affect the cooling performance of hybrid nanofluid spray cooling systems. Other factors such as the hybrid nanofluid thermal conductivity and latent heat of vaporization may have dominant effects on spray cooling performance at low particle concentration (less than 0.1% volume fraction), where a thin and non-uniform residue surface may have little wetting and wicking effects. However, at high particle concentration of hybrid nanofluids (above 0.5% volume fraction), the residue surface properties (such as wetting and wicking) have dominant effect on spray cooling performance as compared to thermal conductivity effects.

4.4. Spray cooling of IGBT power modules for current electric vehicles

It must be noted that all results presented in Section 4.4 and Section 4.5 are based on numerical simulation. Moreover, as both SGHF/MR-2 and CAHF hybrid nanofluid spray systems exhibit dominant critical heat flux (CHF) compared to SGHF/MR-1 spray system at a high mean volumetric flux of 0.019 $m^3/(m^2.s)$ (Figure 6 (b)), the electric vehicle power module cooling analysis (in Section 4.4 and Section 4.5) is only performed for SGHF/MR-2 and CAHF spray cooling systems at 0.1% volume fraction. Figure 8 (a) shows temperature across different layers of an IGBT module without a direct bond copper (DBC) layer. It can be observed that IGBT chip temperature much lower than its failure temperature is achieved using SGHF/MR-2 and CAHF spray cooling systems. On the other hand, deionized water and other dielectric fluids do not efficiently cool the chip to keep it below its failure temperature. This is due to lower heat removal flux and reduced heat transfer coefficient of water and dielectric sprays compared to considered hybrid nanofluid (SGHF/MR-2 and CAHF) sprays, as shown in Table 3. In Figure 8 (b), a similar trend can be observed for IGBT module cooling when the direct bond copper (DBC) is used as a substrate. However, due to added packaging thermal resistance from AlN and lower copper layers, the IGBT chip temperature is higher for power modules using DBC compared to the ones without DBC. Despite an added packaging thermal resistance due to DBC substrate, the hybrid nanofluid spray cooling can still maintain the IGBT chip temperature below its failure temperature, while the same is not achieved for water and dielectric spray cooling, as shown in Figure 8 (b).

Figure 8 (c) illustrates the temperature along the length of an inverter leg (*x*-direction in Figure 1 (c)) over seven IGBT chip and spray surfaces obtained using spray cooling of considered thermal fluids. It can be noticed that SGHF/MR-2 and CAHF spray cooling can maintain the IGBT chip temperature below its failure temperature. However, water and dielectric fluid spray cooling cannot effectively cool an IGBT module thus increasing the risk of its failure. It can be further observed that a uniform chip surface temperature is achieved due to spray cooling technology adopted in this research that can prevent temperature overshoot and localized hotspots thus keeping the overall chip temperature below its failure temperature using considered hybrid nanofluid spray cooling. Moreover, heat flux higher than maximum heat dissipation flux of IGBT modules (500 W/cm^2) can be achieved using both CAHF and SGHF/MR-2 spray cooling (as shown in Table 3) while keeping these devices below their failure temperatures. On the other hand, water and dielectric spray cooling fail to keep an IGBT chip below its failure temperature due to their reduced heat transfer coefficients and low heat flux removal capability.

4.5. Spray cooling of WBG power modules for future electric vehicles

Both CAHF and SGHF/MR-2 are potential candidates for high heat flux removal in wide band gap (WBG) power modules of future electric vehicles (EV’s), as shown in Figure 9. These results suggest that spray cooling using considered hybrid nanofluids (SGHF/MR-2 and CAHF) can keep high power electronics of future EV’s well below their failure temperatures. Despite higher operating temperature limit of WBG chips (up to 250 °C) compared to IGBT chips (up to 150 °C), water and dielectric fluid spray cooling still fail to keep WBG chip temperature below its failure temperature, as illustrated in Figure 9. This is because high heat dissipation flux in WBG chips (1000 W/cm^2 compared to 500 W/cm^2 in IGBT chips) is not effectively removed by water and dielectric fluids due to their poor thermophysical properties and low heat transfer coefficients.

Figure 9 (a, b) shows that a DBC substrate increases the chip temperature compared to a copper substrate, however, the hybrid nanofluid spray cooling can still maintain the WBG chip temperature below its failure temperature. Conversely, a WBG power module cooled by water and dielectric fluid sprays experiences a further increase in chip temperature above its failure temperature when a DBC substrate is used instead of a copper substrate. Even if a copper substrate is used instead of a DBC substrate to reduce the packaging overall thermal resistance, water and dielectric fluid spray cooling still cannot maintain the WBG chip temperature within safe temperature limits (as demonstrated in Figure 9 (a)), making existing fluids inappropriate for thermal management of future EV high power electronics. Figure 9 (c) illustrates that chip surface temperature below its failure temperature is achieved for seven WBG chips along the length of an inverter leg using considered hybrid nanofluid (SGHF/MR-2 and CAHF) spray cooling. On the other hand, water and dielectric fluid spray cooling cannot keep WBG chips below their failure temperatures suggesting an urgent need of advanced thermal fluids (such as hybrid nanofluids) for thermal management of future EV high power electronics.

5. Conclusions

Due to increased power density and immense heat dissipation in high heat flux devices, these devices may not be thermally managed using spray cooling systems based on conventional fluids. To address this challenge, the spray cooling system for the copper-alumina hybrid nanofluid (CAHF) and the silver-graphene hybrid nanofluid (SGHF) was developed in this study and their spray cooling performances were compared with water spray cooling performance. The results showed that the hybrid nanofluid spray cooling system outperforms the water spray system exhibiting the critical heat flux enhancement up to 126% for SGHF/MR-2 spray. The hybrid nanofluid droplet residue formed over a heated copper surface was investigated to determine its effect on the CHF enhancement. Moreover, the hybrid nanofluid spray cooling potential was analyzed on a high heat flux cooling application, that is, the high power electronics of current and future electric vehicles. The following are the main conclusions from this study:

- At a mean volumetric flux of $Q'' = 0.01$ m^3/(m^2.s), the critical heat flux (CHF) is enhanced up to 89%, 106% and 107% for the SGHF/MR-1, SGHF/MR-2 and CAHF spray system compared to water spray system, respectively.

- At a mean volumetric flux of $Q'' = 0.019$ m^3/(m^2.s), the critical heat flux (CHF) is enhanced up to 31.5%, 126% and 100% for the SGHF/MR-1, SGHF/MR-2 and CAHF spray system compared to water spray system, respectively.
- The highest CHF of 611 W/cm^2 is obtained for SGHF/MR-2 spray system at 0.1% volume fraction and mean volumetric flux of $Q'' = 0.019$ m^3/(m^2.s).
- The studied hybrid nanofluid spray systems generally exhibit higher critical surface temperature (T_{sc}) compared to water spray system possibly due to enhanced wettability and wickability of their porous residue surfaces.
- The hybrid nanofluid spray cooling can keep IGBT and WBG power modules below their failure temperatures of 150 °C and 250 °C, respectively. Conversely, water and dielectric fluids fail to cool both IGBT and WBG power modules below their failure temperatures.

Acknowledgements

The funding for this research is provided by the Hong Kong PhD Fellowship Scheme (HKPFS), the Hong Kong Research Grant Council via Collaborative Research Fund (CRF) account C6022-16G, General Research Fund (GRF) accounts 16206918 & 17205419 and Early Career Scheme (ECS) account 21200819.

References

[1] K.A. Estes, I. Mudawar, Comparison of Two-Phase Electronic Cooling Using Free Jets and Sprays, J. Electron. Packag. 117 (1995) 323–332. https://doi.org/10.1115/1.2792112.

[2] S.G. Kandlikar, A. V Bapat, Evaluation of Jet Impingement, Spray and Microchannel Chip Cooling Options for High Heat Flux Removal, Heat Transf. Eng. 28 (2007) 911–923. https://doi.org/10.1080/01457630701421703.

[3] Y. Xia, X. Gao, R. Li, Management of surface cooling non-uniformity in spray cooling, Appl. Therm. Eng. 180 (2020) 115819. https://doi.org/https://doi.org/10.1016/j.applthermaleng.2020.115819.

[4] S. Khandekar, G. Sahu, K. Muralidhar, E.Y. Gatapova, O.A. Kabov, R. Hu, X. Luo, L. Zhao, Cooling of high-power LEDs by liquid sprays: Challenges and prospects, Appl. Therm. Eng. 184 (2021) 115640. https://doi.org/https://doi.org/10.1016/j.applthermaleng.2020.115640.

[5] G. Liang, I. Mudawar, Review of spray cooling – Part 1: Single-phase and nucleate boiling regimes, and critical heat flux, Int. J. Heat Mass Transf. 115 (2017) 1174–1205.

https://doi.org/10.1016/j.ijheatmasstransfer.2017.06.029.

[6] P. Liu, R. Kandasamy, J.Y. Ho, J. Xie, T.N. Wong, Experimental study on heat transfer enhancement using combined surface roughening and macro-structures in a confined double-nozzle spray cooling system, Appl. Therm. Eng. 202 (2022) 117850. https://doi.org/https://doi.org/10.1016/j.applthermaleng.2021.117850.

[7] S. Jones-jackson, S. Member, R. Rodriguez, A. Emadi, Jet Impingement Cooling in Power Electronics for Electrified Automotive Transportation : Current Status and Future Trends, IEEE Trans. Power EEectronics. 8993 (2021) 1–16. https://doi.org/10.1109/TPEL.2021.3059558.

[8] C. Qian, A.M. Gheitaghy, J. Fan, H. Tang, B. Sun, H. Ye, G. Zhang, Thermal Management on IGBT Power Electronic Devices and Modules, IEEE Access. 6 (2018) 12868–12884. https://doi.org/10.1109/ACCESS.2018.2793300.

[9] I. Mudawar, D. Bharathan, K. Kelly, S. Narumanchi, Two-Phase Spray Cooling of Hybrid Vehicle Electronics, IEEE Trans. Components Packag. Technol. 32 (2009) 501–512.

[10] K.W. Jung, C.R. Kharangate, H. Lee, J. Palko, F. Zhou, M. Asheghi, E.M. Dede, K.E. Goodson, Microchannel cooling strategies for high heat flux (1 kW/cm2) power electronic applications, in: 2017 16th IEEE Intersoc. Conf. Therm. Thermomechanical Phenom. Electron. Syst., 2017: pp. 98–104. https://doi.org/10.1109/ITHERM.2017.7992457.

[11] Heterogenous Integration Roadmap, (2019) 1–23. https://eps.ieee.org/technology/heterogeneous-integration-roadmap.html (accessed April 25, 2021).

[12] R. Singh, M. Mochizuki, T. Yamada, T. Nguyen, Cooling of LED headlamp in automotive by heat pipes, Appl. Therm. Eng. 166 (2020) 114733. https://doi.org/https://doi.org/10.1016/j.applthermaleng.2019.114733.

[13] A. Christensen, S. Graham, Thermal effects in packaging high power light emitting diode arrays, Appl. Therm. Eng. 29 (2009) 364–371. https://doi.org/https://doi.org/10.1016/j.applthermaleng.2008.03.019.

[14] T. Steiner, R. Sittig, IGBT module setup with integrated micro-heat sinks, IEEE Int. Symp. Power Semicond. Devices ICs. (2000) 209–212. https://doi.org/10.1109/ispsd.2000.856808.

[15] Y. Avenas, C. Gillot, A. Bricard, C. Schaeffer, On the use of flat heat pipes as thermal spreaders in power electronics cooling, in: 2002 IEEE 33rd Annu. IEEE Power Electron. Spec. Conf. Proc. (Cat. No.02CH37289), 2002: pp. 753–757 vol.2. https://doi.org/10.1109/PSEC.2002.1022544.

[16] C. Gillot, C. Schaeffer, A. Bricard, Integrated micro heat sink for power multichip module, in: Conf. Rec. 1998 IEEE Ind. Appl. Conf. Thirty-Third IAS Annu. Meet. (Cat. No.98CH36242), 1998: pp. 1046–1050 vol.2. https://doi.org/10.1109/IAS.1998.730275.

[17] M.C. Shaw, J.R. Waldrop, S. Chandrasekaran, B. Kagalwala, X. Jing, E.R. Brown, V.J. Dhir, M. Fabbeo, Enhanced thermal management by direct water spray of high-voltage,

high power devices in a three-phase, 18-hp AC motor drive demonstration, in: ITherm 2002. Eighth Intersoc. Conf. Therm. Thermomechanical Phenom. Electron. Syst. (Cat. No.02CH37258), 2002: pp. 1007–1014. https://doi.org/10.1109/ITHERM.2002.1012567.

[18] R. Kumar, B. Tiwary, P.K. Singh, Thermofluidic analysis of Al2O3-water nanofluid cooled branched wavy heat sink, Appl. Therm. Eng. 201 (2022) 117787. https://doi.org/https://doi.org/10.1016/j.applthermaleng.2021.117787.

[19] C.Y. Tso, C.Y.H. Chao, Study of enthalpy of evaporation, saturated vapor pressure and evaporation rate of aqueous nanofluids, Int. J. Heat Mass Transf. 84 (2015) 931–941. https://doi.org/10.1016/j.ijheatmasstransfer.2015.01.090.

[20] S. Fu, C. Tso, Y. Fong, C.Y.H. Chao, Evaporation of Al2O3-water nanofluids in an externally micro-grooved evaporator, Sci. Technol. Built Environ. 23 (2017) 345–354. https://doi.org/10.1080/23744731.2016.1250562.

[21] C.Y. Tso, S.C. Fu, C.Y.H. Chao, A semi-analytical model for the thermal conductivity of nanofluids and determination of the nanolayer thickness, Int. J. Heat Mass Transf. 70 (2014) 202–214. https://doi.org/https://doi.org/10.1016/j.ijheatmasstransfer.2013.10.077.

[22] K. Nemade, S. Waghuley, A novel approach for enhancement of thermal conductivity of CuO/H2O based nanofluids, Appl. Therm. Eng. 95 (2016) 271–274. https://doi.org/https://doi.org/10.1016/j.applthermaleng.2015.11.053.

[23] S.-S. Hsieh, H.-Y. Leu, H.-H. Liu, Spray cooling characteristics of nanofluids for electronic power devices., Nanoscale Res. Lett. 10 (2015) 139. https://doi.org/10.1186/s11671-015-0793-7.

[24] H. Bellerova, M. Pohanka, M. Raudensky, A.A. Tseng, Spray cooling by Al2O3 and TiO2 nanoparticles in water, in: 2010 12th IEEE Intersoc. Conf. Therm. Thermomechanical Phenom. Electron. Syst., 2010: pp. 1–5. https://doi.org/10.1109/ITHERM.2010.5501333.

[25] H. Bellerová, A.A. Tseng, M. Pohanka, M. Raudensky, Heat transfer of spray cooling using alumina/water nanofluids with full cone nozzles, Heat Mass Transf. 48 (2012) 1971–1983. https://doi.org/10.1007/s00231-012-1037-3.

[26] A.A. Tseng, H. Bellerová, M. Pohanka, M. Raudensky, Effects of titania nanoparticles on heat transfer performance of spray cooling with full cone nozzle, Appl. Therm. Eng. 62 (2014) 20–27. https://doi.org/https://doi.org/10.1016/j.applthermaleng.2013.07.023.

[27] J.A.R. Babu, K.K. Kumar, S.S. Rao, State-of-art review on hybrid nanofluids, Renew. Sustain. Energy Rev. 77 (2017) 551–565. https://doi.org/10.1016/j.rser.2017.04.040.

[28] M.J. Nine, H. Chung, M.R. Tanshen, N.A.B.A. Osman, H. Jeong, Is metal nanofluid reliable as heat carrier?, J. Hazard. Mater. 273 (2014) 183–191. https://doi.org/10.1016/j.jhazmat.2014.03.055.

[29] V. Kumar, J. Sarkar, Particle ratio optimization of Al2O3-MWCNT hybrid nanofluid in minichannel heat sink for best hydrothermal performance, Appl. Therm. Eng. 165 (2020) 114546. https://doi.org/https://doi.org/10.1016/j.applthermaleng.2019.114546.

[30] F.R. Siddiqui, C.Y. Tso, K.C. Chan, S.C. Fu, C.Y.H. Chao, On trade-off for dispersion stability and thermal transport of Cu-Al2O3 hybrid nanofluid for various mixing ratios, Int. J. Heat Mass Transf. 132 (2019) 1200–1216. https://doi.org/https://doi.org/10.1016/j.ijheatmasstransfer.2018.12.094.

[31] F.R. Siddiqui, C.Y. Tso, S.C. Fu, H.H. Qiu, C.Y.H. Chao, Evaporation and wetting behavior of silver-graphene hybrid nanofluid droplet on its porous residue surface for various mixing ratios, Int. J. Heat Mass Transf. 153 (2020) 119618. https://doi.org/https://doi.org/10.1016/j.ijheatmasstransfer.2020.119618.

[32] A. Bhattad, J. Sarkar, P. Ghosh, Experimentation on effect of particle ratio on hydrothermal performance of plate heat exchanger using hybrid nanofluid, Appl. Therm. Eng. 162 (2019) 114309. https://doi.org/https://doi.org/10.1016/j.applthermaleng.2019.114309.

[33] M.R. Han, Z. H, Yang, B., Kim, S. H., Zachariah, Application of hybrid sphere/carbonnanotube particles in nanofluids, Nanotechnology. 18 (2007) 105–109.

[34] F.R. Siddiqui, C.Y. Tso, S.C. Fu, C.Y.H. Chao, H.H. Qiu, Experimental Investigation On Silver-Graphene Hybrid Nanofluid Droplet Evaporation And Wetting Characteristics Of Its Nanostructured Droplet Residue, in: Proc. ASME-JSME-KSME 8th Jt. Fluids Eng. Conf., San Francisco, California, USA. July 28–August 1, 2019. Paper No: AJKFluids2019-5049, V004T06A010, 2019. https://doi.org/https://doi.org/10.1115/AJKFluids2019-5049.

[35] F.R. Siddiqui, C.Y. Tso, S.C. Fu, H.H. Qiu, C.Y.H. Chao, Droplet evaporation and boiling for different mixing ratios of the silver-graphene hybrid nanofluid over heated surfaces, Int. J. Heat Mass Transf. 180 (2021) 121786. https://doi.org/https://doi.org/10.1016/j.ijheatmasstransfer.2021.121786.

[36] A. Miric, M. Sc, P. Dietrich, M. Sc, H. Germany, Inorganic Substrates for Power Electronics Applications, (n.d.) 1–7.

[37] B. Li, H. Kuo, X. Wang, Y. Chen, Y. Wang, D. Gerada, S. Worall, I. Stone, Thermal Management of Electrified Propulsion System for Low - Carbon Vehicles, Automot. Innov. 3 (2020) 299–316. https://doi.org/10.1007/s42154-020-00124-y.

[38] W. Jia, H. Qiu, Experimental investigation of droplet dynamics and heat transfer in spray cooling, Exp. Therm. Fluid Sci. 27 (2003) 829–838. https://doi.org/10.1016/S0894-1777(03)00015-3.

[39] M.O. Panão, A.S. Moita, A.L. Moreira, On the Statistical Characterization of Sprays, Appl. Sci. . 10 (2020). https://doi.org/10.3390/app10176122.

[40] F.R. Siddiqui, C.Y. Tso, S.C. Fu, H. Qiu, C.Y.H. Chao, Droplet Evaporation of Cu–Al2O3 Hybrid Nanofluid Over Its Residue and Copper Surfaces: Toward Developing a New Analytical Model, J. Heat Transfer. 143 (2021) 1–11. https://doi.org/10.1115/1.4048970.

[41] A. Al-Sharafi, A.Z. Sahin, B.S. Yilbas, S.Z. Shuja, Marangoni convection flow and heat

transfer characteristics of water–CNT nanofluid droplets, Numer. Heat Transf. Part A Appl. 69 (2016) 763–780. https://doi.org/10.1080/10407782.2015.1090809.

[42] K.A. Estes, I. Mudawar, Correlation of Sauter mean diameter and critical heat flux for spray cooling of small surfaces, Int. J. Heat Mass Transf. 38 (1995) 2985–2996. https://doi.org/10.1016/0017-9310(95)00046-C.

[43] G. Liang, I. Mudawar, Review of spray cooling – Part 1: Single-phase and nucleate boiling regimes, and critical heat flux, Int. J. Heat Mass Transf. 115 (2017) 1174–1205. https://doi.org/10.1016/j.ijheatmasstransfer.2017.06.029.

[44] J.R. Rybicki, I. Mudawar, Single-phase and two-phase cooling characteristics of upward-facing and downward-facing sprays, Int. J. Heat Mass Transf. 49 (2006) 5–16. https://doi.org/https://doi.org/10.1016/j.ijheatmasstransfer.2005.07.040.

[45] C. Cho, R. Ponzel, Experimental study on the spray cooling of a heated solid surface, in: Am. Soc. Mech. Eng. Fluids Eng. Div. FED, 1997: pp. 265–272. https://www.scopus.com/inward/record.uri?eid=2-s2.0-0031369786&partnerID=40&md5=39b6c4c7752c457df3ec5df51ec23b80.

[46] I. Mudawar, W.S. Valentine, Determination of the local quench curve for spray-cooled metallic surfaces, J. Heat Treat. 7 (1989) 107–121. https://doi.org/10.1007/BF02833195.

[47] Tesla Roadster and Model S Inverter, (n.d.). https://www.pntpower.com/on-tesla-electric-vehicles-semiconductor-packaging/ (accessed April 29, 2021).

Table 1 Measured latent heat of vaporization (h_{fg}) for different hybrid nanofluid particle concentration (volume fraction) measured using Differential Scanning Calorimetry (Q1000, TA Instruments, USA). Measured h_{fg} for water is 2259±25.81 kJ/kg.

Hybrid nanofluid	Latent heat of vaporization, h_{fg} (kJ/kg)/ Boiling Point (°C)			
	φ = 0.01%	φ = 0.1%	φ = 0.5%	φ = 1.0%
SGHF/MR-1	2395.6±59.5/101.07±0.08	2207.8±47.2/100.92±0.09	2395.7±54/99.97±0.12	2149.8±53.5/98.79±0.07
SGHF/MR-2	2199.5±42.2/100.31±0.09	2325.5±31.7/101.52±0.13	2270.3±50.1/99.47±0.11	2120.2±36.6/99.45±0.08
CAHF	2373.1±56.6/99.85±0.12	2330.1±48.3/101.77±0.07	2352.6±44.1/101.32±0.14	2081.8±30.5/101.3±0.12

Table 2 The hybrid nanofluid droplet residue properties at 0.1% volume fraction.

Hybrid nanofluid droplet residue	Static contact angle, θ (deg)	Surface free energy, γ_{sv} (mN/m)	Average surface roughness, R_a (μm)	Mean pore (Feret) diameter, $\emptyset_f$ (μm)
SGHF/MR-1	5.06±1.13	57.18±1.20	2.58±0.80	0.672±0.031
SGHF/MR-2	65.28±1.88	48.51±1.35	2.20±0.04	0.533±0.015
CAHF	19.43±0.80	40.46±1.98	7.16±0.71	0.275±0.013

Table 3 Spray cooling characteristics of hybrid nanofluids (at 0.1% volume fraction) compared to existing thermal fluids.

Fluid	Mean volumetric flux, Q'' ($m^3/(m^2.s)$)	Saturation temperature, T_{sat} (°C)	$T_{sat} - T_f$, ΔT (°C)	Latent heat of vaporization, h_{fg} (kJ/kg)	Critical heat flux, q' (W/cm^2)	Heat transfer coefficient, h ($W/m^2.K$)
SGHF/MR-2	0.019	101.5	55	2325.5	611	111091
CAHF	0.019	101.8	55	2330.1	542	98545
H_2O	0.019	100	60	2259	270	45000
HFE-7100 [9]	0.037	60.4	40.6	112.1	138	33990
FC-72 [42]	0.021	57.3	33	88	93	28182

Table 4 Comparison of spray efficiency and Nusselt number for hybrid nanofluid spray and water spray systems.

	Spray Efficiency, η	Nusselt Number, Nu			
Fluid	$\boldsymbol{\eta = q'/\rho_f Q''(h_{fg} + C_p \Delta T)}$	Present Study $Nu=hd_{32}/k$	Mudawar and Valentine [46] $Nu=2.512(Re^{0.76}Pr^{0.56})$	Rybicki and Mudawar [44] $Nu=4.7(Re^{0.61}Pr^{0.32})$	Cho and Ponzel [45] $Nu=2.531(Re^{0.667}Pr^{0.309})$
SGHF/MR-2	12.6	38.9	21.1	40.3	35.9
CAHF	11.1	34.5	21.26	40.7	36.1
H_2O	5.6	16.0	21.6	41.6	36.3

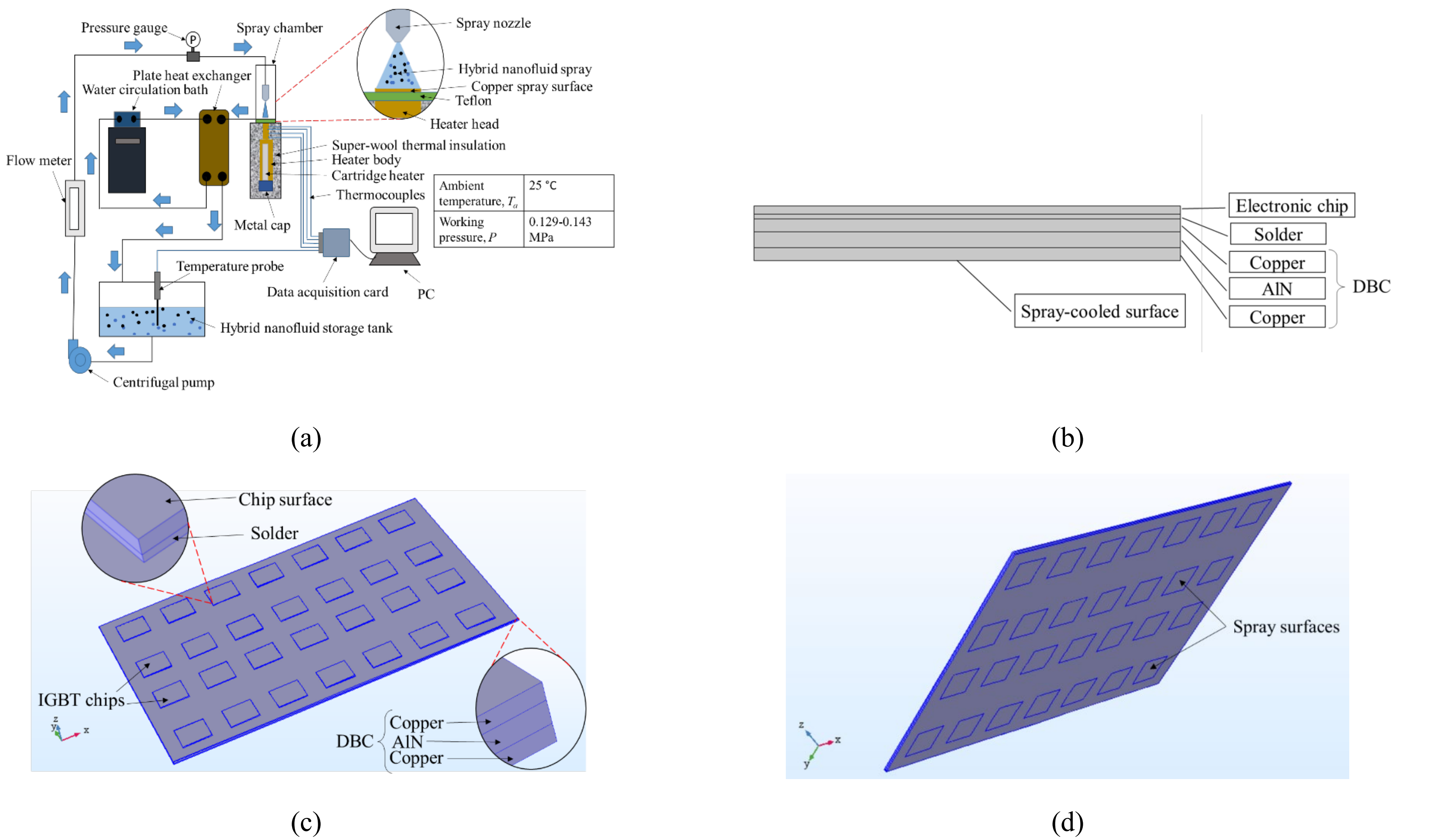

Figure 1(a) Schematic of the hybrid nanofluid spray cooling experimental setup, (b) A 2-D model of an IGBT power module, (c) inverter leg front-side comprising 28 IGBT chips (used in Tesla Roadster and Model S [47]) and (d) inverter leg backside comprising spray cooling surfaces.

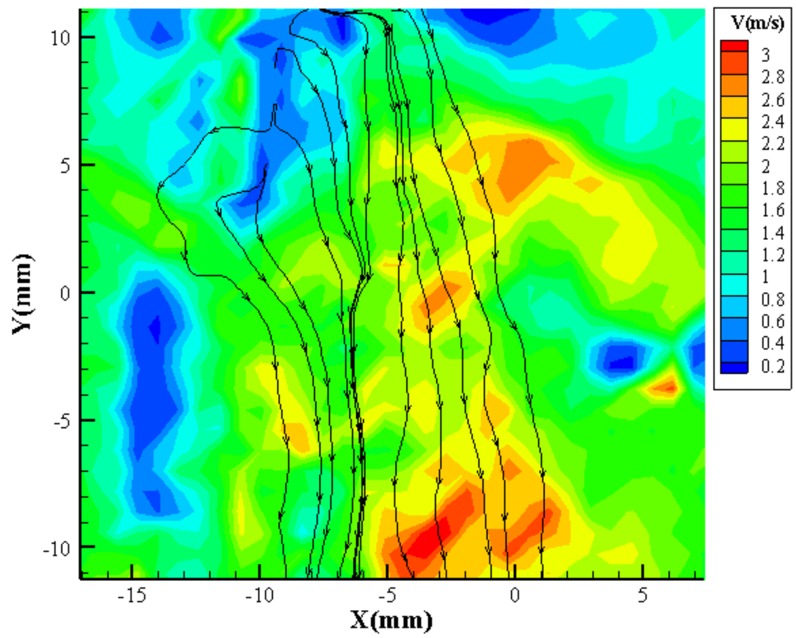

(a)

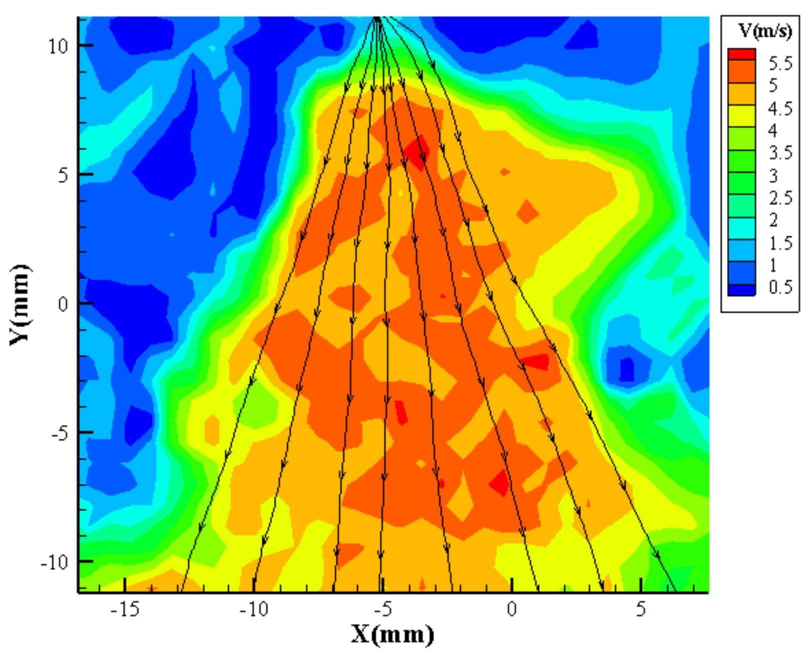

(b)

Figure 2 Spray velocity field at a mean volumetric flux of (a) Q" = 0.01 $m^3/(m^2.s)$ and (b) Q" = 0.019 $m^3/(m^2.s)$.

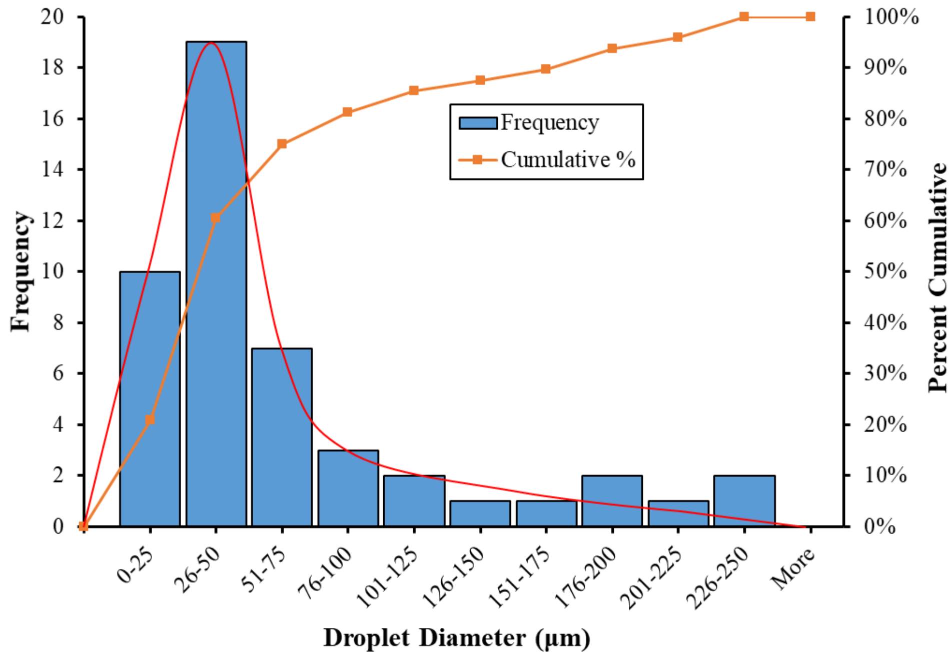

(a)

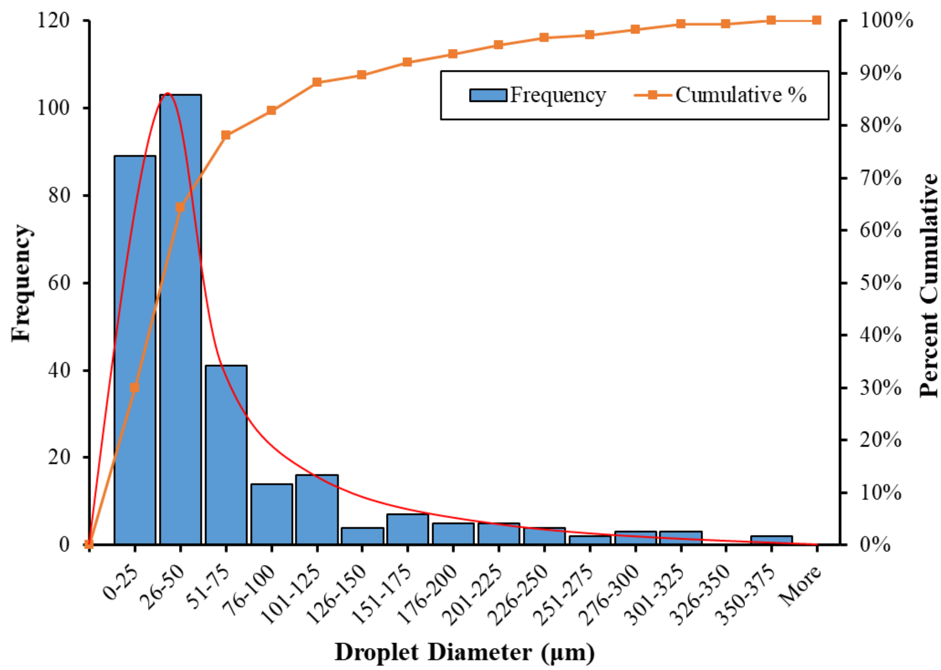

(b)

Figure 3 Spray droplet size distribution for a mean volumetric flux of (a) Q" = 0.01 $m^3/(m^2.s)$ and (b) Q" = 0.019 $m^3/(m^2.s)$.

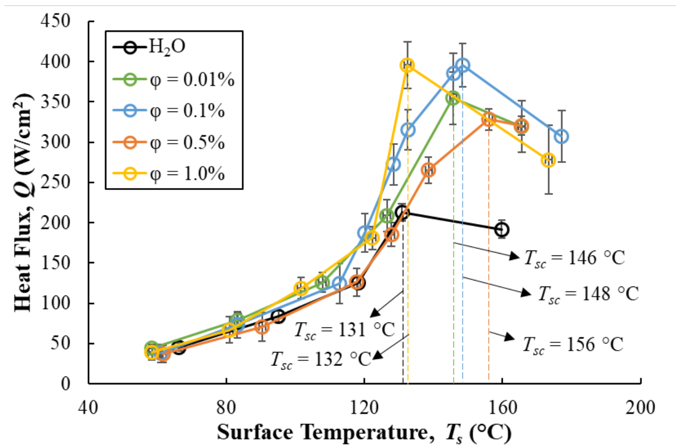

(a)

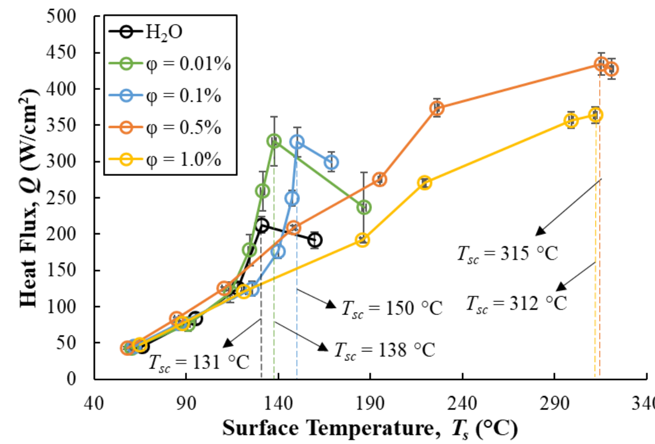

(b)

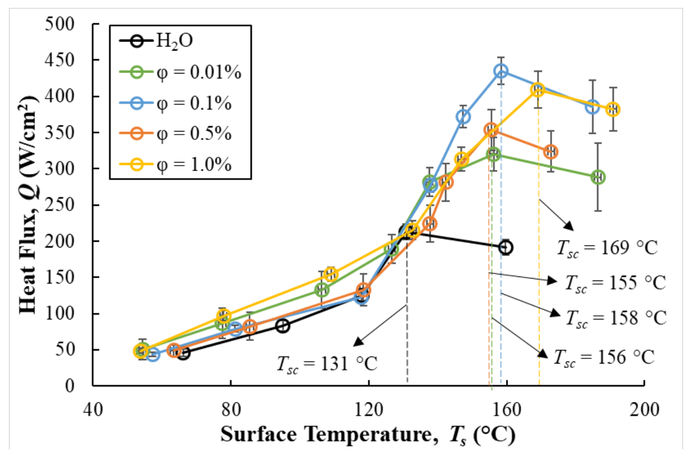

(c)

Figure 4 Heat flux for (a) SGHF/MR-1, (b) SGHF/MR-2 and (c) CAHF spray cooling at a mean volumetric flux of $Q'' = 0.01$ $m^3/(m^2.s)$.

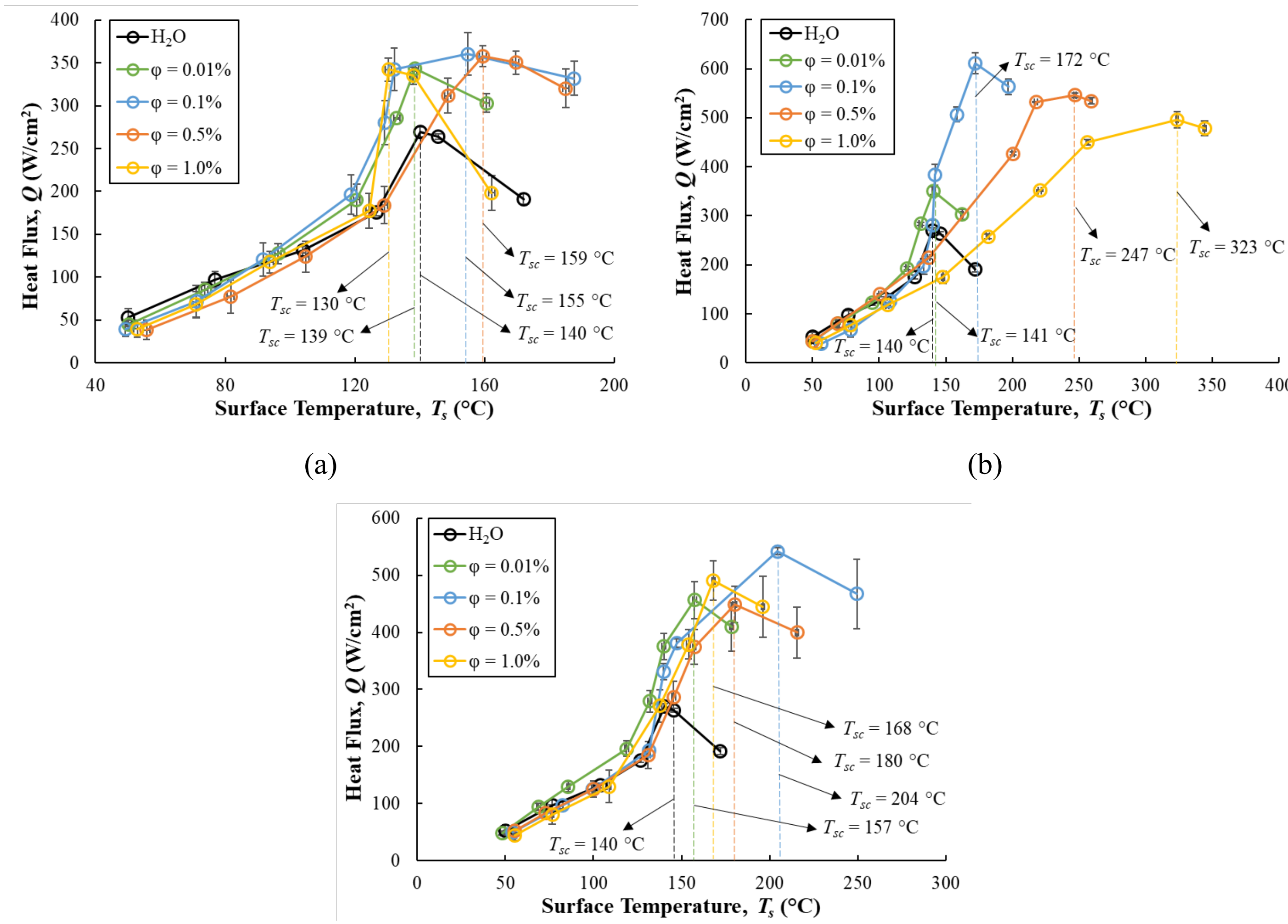

(a) (b) (c)

Figure 5 Heat flux for (a) SGHF/MR-1, (b) SGHF/MR-2 and (c) CAHF spray cooling at a mean volumetric flux of Q" = 0.019 $m^3/(m^2 s)$.

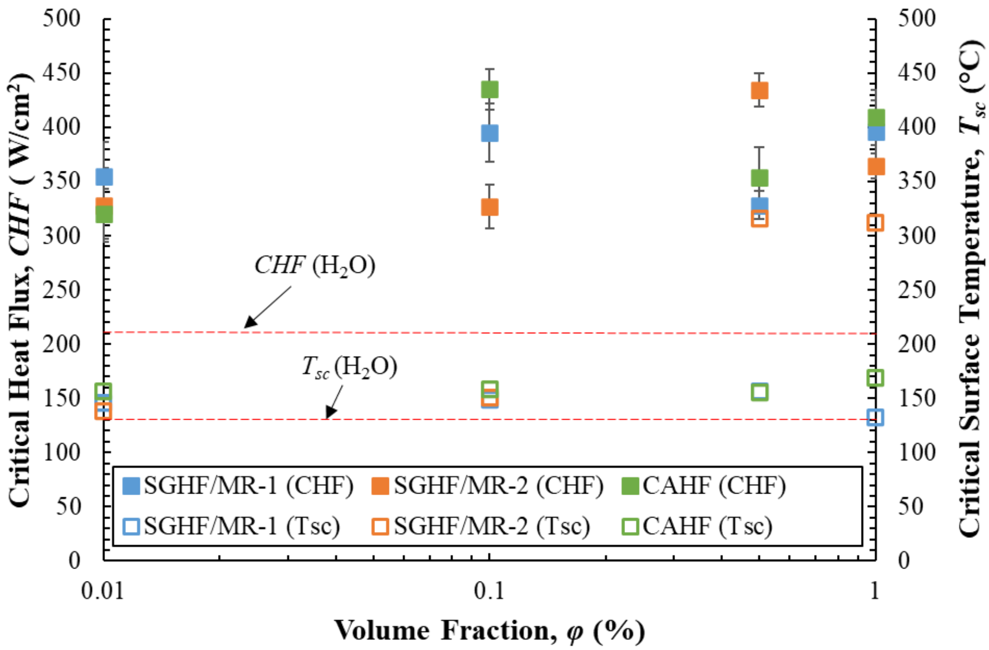

(a)

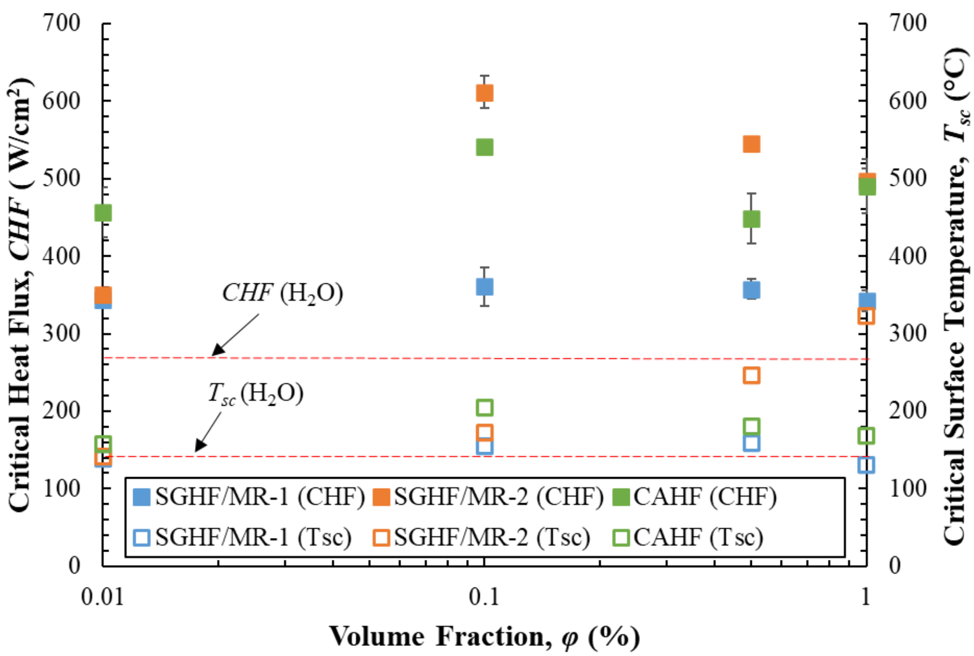

(b)

Figure 6 Critical heat flux (CHF) and critical surface temperature (T_{sc}) for different volume fractions of SGHF (MR-1 and MR-2) and CAHF spray cooling at a mean volumetric flux of (a) $Q" = 0.01$ m^3/(m^2.s) and (b) $Q" = 0.019$ m^3/(m^2.s).

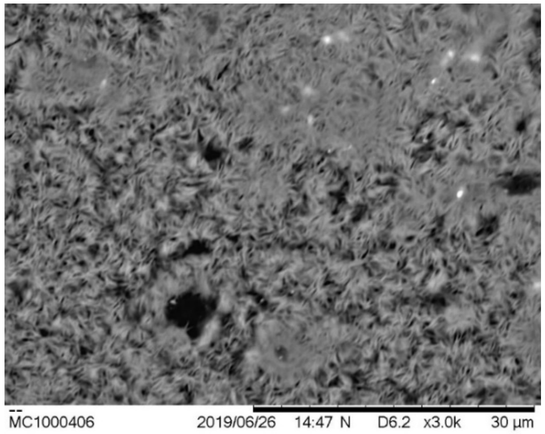

(a)

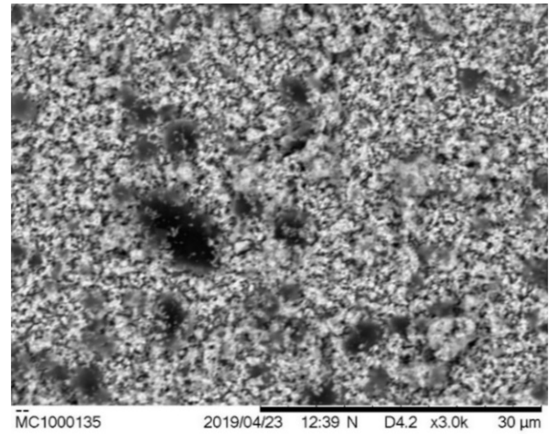

(b)

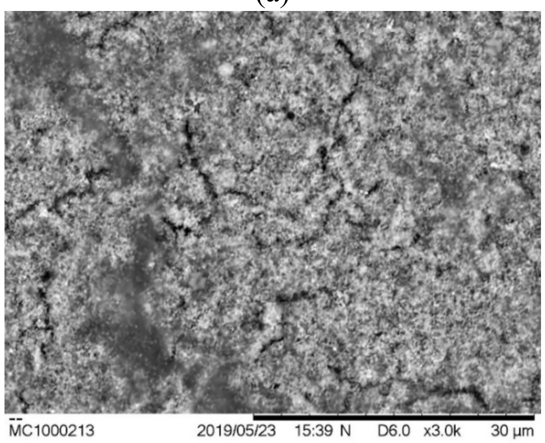

(c)

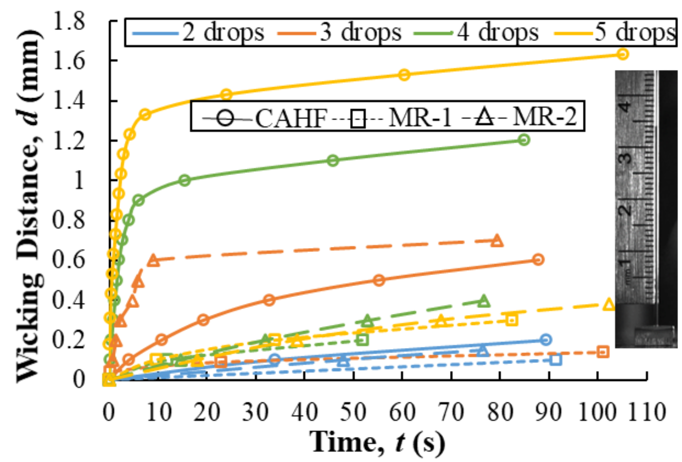

(d)

Figure 7 SEM micrographs showing residue surfaces obtained from 150 µl volume of (a) SGHF/MR-1, (b) SGHF/MR-2 and (c) CAHF droplet at 0.1% volume fraction on a copper surface at T_s = 100 °C, (d) comparison of wicking distance for CAHF, MR-1 and MR-2 residues obtained from 2−5 droplets of 150 µl volume each at 0.1% volume fraction on a copper surface.

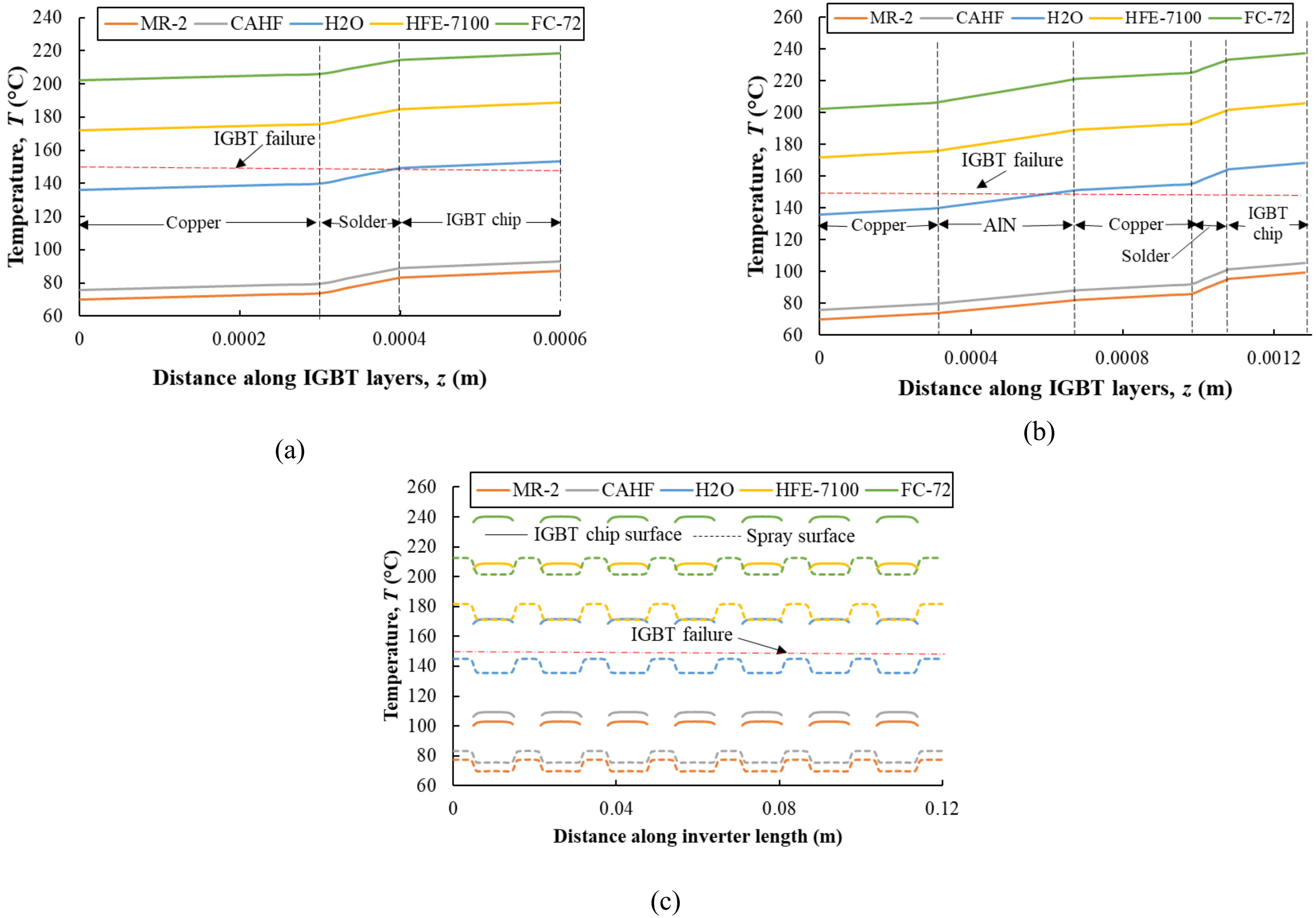

Figure 8 Temperature across an IGBT module (a) without a direct bond copper (DBC) and (b) with direct bond copper. (c) Temperature along the length of an inverter leg over 7 IGBT chip surfaces and spray surfaces (inverter backside).

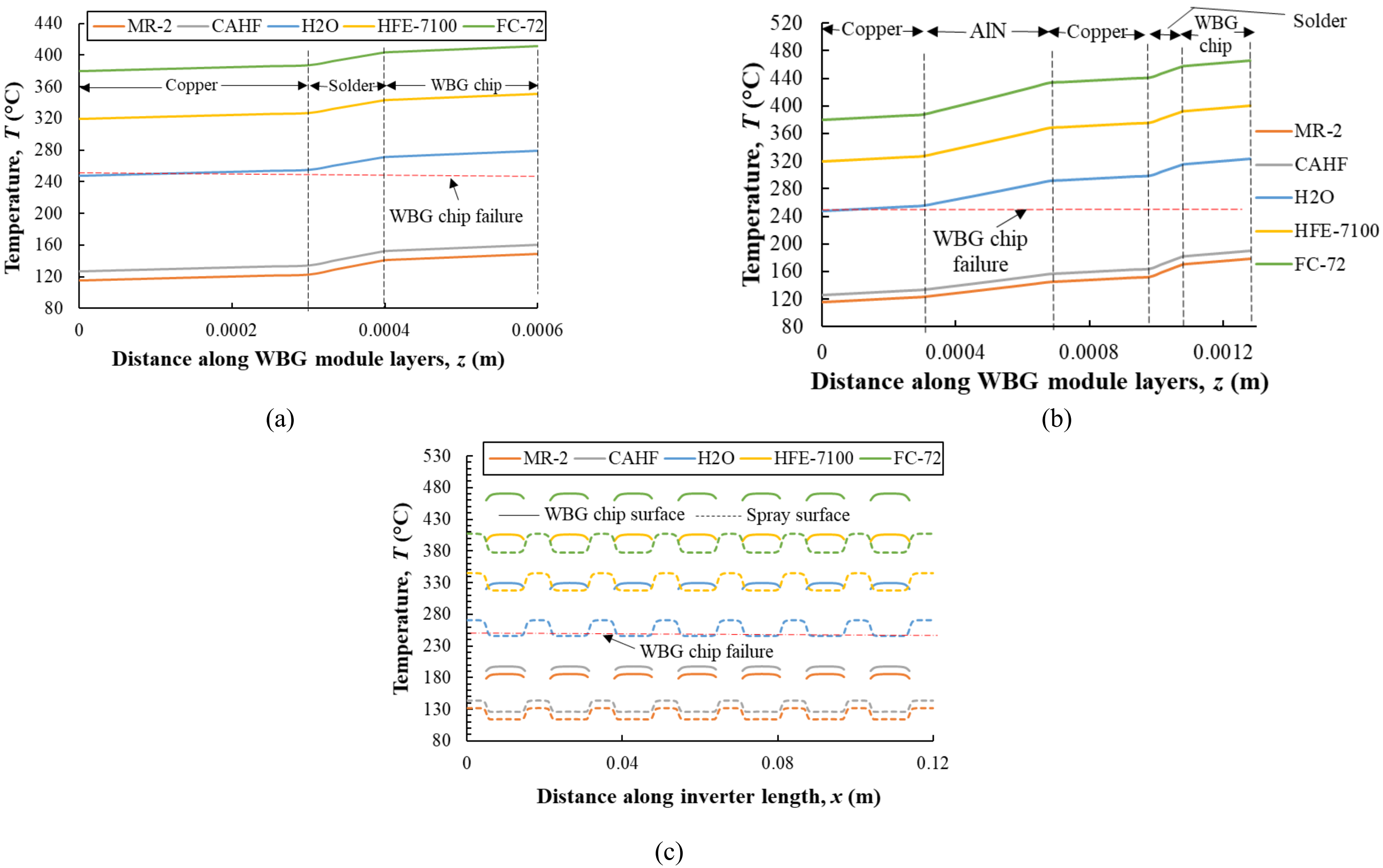

Figure 9 Temperature across WBG chip module (a) without a direct bond copper (DBC) and (b) with direct bond copper (DBC). (c) Temperature distribution along the length of an inverter leg over 7 WBG chip surfaces and spray surfaces (inverter backside)